ADVANCED MATERIALS

Supporting Information

for *Adv. Mater.*, DOI 10.1002/adma.202308522

Suppressing Buried Interface Nonradiative Recombination Losses Toward High-Efficiency Antimony Triselenide Solar Cells

*Guojie Chen, Yandi Luo, Muhammad Abbas, Muhammad Ishaq, Zhuanghao Zheng, Shuo Chen, Zhenghua Su, Xianghua Zhang, Ping Fan and Guangxing Liang**

Supporting Information

Suppressing Buried Interface Nonradiative Recombination Losses Towards High-efficiency Antimony Triselenide Solar Cells

*Guojie Chen, Yandi Luo, Muhammad Abbas, Muhammad Ishaq, Zhuanghao Zheng, Shuo Chen, Zhenghua Su, Xianghua Zhang, Ping Fan, Guangxing Liang**

Supplementary Notes

Supplementary Note1

Texture coefficient (TC) calculation was calculated in order to evaluate the orientation control more intuitively. The TC of the major diffraction peaks was determined using the following equation[1, 2]:

$$TC_{hkl} = \frac{I_{(hkl)}}{I_{0(hkl)}} \Big/ \left(\frac{1}{N}\sum_{i=1}^{N}\frac{I_{(h_i k_i l_i)}}{I_{0(h_i k_i l_i)}}\right) \quad (1\text{-}1)$$

Where $I_{(hkl)}$ and $I_{0(hkl)}$ represent the diffraction peak intensities of [hkl] planes in the measured and standard XRD pattern of Sb_2Se_3, respectively.

Ten diffraction peaks were selected for the TC calculation. A high TC value of a diffraction peak signifies a favored orientation in that direction. It was observed that

when the thickness of the WO_3 layer was fixed at 15 nm, the sample exhibited higher TC values for the (002), (211), and (221) peaks. This indicates that the buried interface modulation induced the orientation control.

Supplementary Note2

The UPS measurements were carried out to estimate the cutoff edge (E_{cutoff}) and the energy gaps (E_{onset}) of the samples. The E_{cutoff} values of binding energy near the surfaces of the SW0 and SW15 samples were 16.39 and 16.49 eV, respectively, and these values for the CdS and CdS-Al samples were 16.29 and 16.94 eV, respectively. Moreover, based on the extrapolation of the linear region of low binding energy, the E_{onset} values of the SW0 and SW15 samples were 0.50 and 0.43 eV, respectively, and the values of CdS and CdS-Al samples were 1.51 and 1.85 eV, respectively. From these obtained values, the conduction band (E_C), valence band (E_V), and Fermi levels (E_F) were calculated utilizing the following equation [3, 4]:

$$\varphi = h\nu - E_{cutoff} \tag{2-1}$$

$$E_v = E_{onset} + E_{onset} \tag{2-2}$$

$$E_c = E_v - E_g \tag{2-3}$$

Where φ represents the work function, $h\nu$ represents the UV photoelectron energy of 21.22 eV. Utilizing these calculated values, the band alignment of the Sb_2Se_3 absorber and the CdS buffer layer could be estimated. It is observed that the buried interface modulation enhances the quality of the Sb_2Se_3 layer and improves the P-type conductivity characteristic. Additionally, the doping treatment of the CdS buffer

layers can increase the carrier density and optimize the band alignment with the absorber layer.

Supplementary Note3

The V_{OC} of a solar cell is significantly dependent on the diode ideality factor (A) and reverse saturation current (J_0) based on the following equation [5]:

$$V_{OC} = \frac{AkT}{q} \ln(\frac{J_{SC}}{J_0} + 1) \quad (3\text{-}1)$$

The J_0 and A could be obtained from the dark J-V characteristic curves. The dark J-V measurement was conducted in a dark environment with a bias voltage of –0.5 to 1 V. The parameters were determined using the following single exponential diode equation[6]:

$$J = J_0 \exp\left[\frac{q}{AkT}(V - JR)\right] + GV - J_L \quad (3\text{-}2)$$

Firstly, the shunt conductance (G) values were extracted from the flat regions of the dJ/dV vs V plot, as shown in Figure S16b. The G values obtained for the SW0, SW15, and SW15-Al samples were 0.0629, 0.0421, and 0.0222 mS/cm^2, respectively. Next, by analyzing the plot of dV/dJ against $(J+J_{SC})^{-1}$, displayed in Figure S16c. The series resistance (R) and A were determined. The intercept of the y-axis provided the values of R, which were found to be 10.33, 5.34, and 4.58 Ω cm^2 for the SW0, SW15, and SW15-Al devices, respectively. Likewise, the slope of AkT/q gave the value of A, which was estimated as 1.81, 1.63, and 1.21 for the SW0, SW15, and SW15-Al devices, respectively. furthermore, the plot of $\ln(J+J_{SC}-GV)$ against $V–RJ$ (Figure

S16d) was used to extract the reverse saturation current J_0. The J_0 values obtained for the SW0, SW15, and SW15-Al devices were estimated to be 2.8×10^{-4}, $7.7 \times 10^{-5,}$ and 1.6×10^{-5} mA/cm^2, respectively. The observed values of J_0 show that the application of dual interface modulation was successful in passivating the interface and surface recombination. It is evident from the experimental results that the V_{OC} of the device is greatly influenced by the diode ideality factor (A) and the reverse saturation current (J_0). These values were determined using dark J-V measurements and the single exponential diode equation. The shunt conductance (G), series resistance (R), and J_0 for each device (SW0, SW15, and SW15-Al) were also obtained and compared. The results highlight the effectiveness of dual interface modulation in mitigating interface and surface recombination.

Supplementary Note4

The logarithmic J-V curves of the three devices are depicted in Figure S17. There are three regimes that the curves fall into: the ohmic zone (at low voltages, exponent n = 1), the trap-filled limit (TFL) region (at intermediate voltages, n > 3), and the trap-free Child region (at high voltages, n > 2). When the bias voltage in the TFL region exceeds the kink point, the current snappishly increases, indicating that all the injected carriers have been injected into the trap states. The space charge-limited current model was employed to study the trap density of the solar cells. Thus, the trap density N_{trap} can be estimated based on the following equation[7]:

$$N_{trap} = \frac{2\varepsilon_0 \varepsilon_r V_{TFL}}{qL^2} \quad (4\text{-}1)$$

Where q is the elementary charge, L is the thickness of the Sb_2Se_3 thin film, ε_r is the relative permutation, and ε_0 is the vacuum permittivity.

Supplementary Note5:

Temperature-dependent *J-V* measurement was performed to quantify the blocking barrier heights of the back contact. The barrier heights were derived from the following equation [8]:

$$R_S = R_0 + (k/qA^*T) \times \exp(\Phi_B/kT) \quad (5\text{-}1)$$

Where Φ_B is the blocking contact barrier height and A^* is the effective Richardson constant. Thus, the Φ_B values can be obtained by fitting the corresponding linear region of the plot of $\ln(R_S T)$ against $1/T$.

Besides, the activation energy (E_A) of the dominant recombination path was derived by plotting $A\ln(J_0)$ and $1/kT$, according to the following equation [9]:

$$Aln(J_0) = Aln(J_{00}) - E_A/kT \quad (5\text{-}2)$$

Where J_0 is the reverse saturation current density, J_{00} is the pre-factor dependent on the recombination path, A is the ideal factor, k is the Boltzmann constant, T is the temperature and E_A is the carrier recombination activation energy. One can determine the primary recombination pathway by comparing the activation energy values with the band gap value of the absorber layer. When E_A is near to E_g, bulk recombination is evident; when E_A is smaller than E_g, interface recombination is evident.

Supplementary Note6:

The doping density $N_{C\text{-}V}$ measured by the *C–V* profiling includes free carriers, bulk defects, and interfacial defects, whereas the DLCP-measured doping density N_{DLCP} only includes free carriers and bulk defects. Hence, the interfacial defects of the device could be calculated via $N_{C\text{-}V} - N_{DLCP}$. The plots of $N_{C\text{-}V}$ and N_{DLCP} against the profiling width x can be obtained by the following equations[10]:

$$N_{C-V} = \frac{-2\varepsilon_{r,n}N_D}{\left(\frac{d(1/C^2)}{dV}\right)qA^2\varepsilon_0\varepsilon_{r,n}\varepsilon_{r,p}N_D + 2\varepsilon_{r,p}} \tag{6-1}$$

$$N_{DLCP} = -\frac{C_0^3}{2q\varepsilon_0\varepsilon_{r,p}A^2C_1} \tag{6-2}$$

$$W_d = \frac{\varepsilon_0\varepsilon_{r,p}A}{C_0} \tag{6-3}$$

where N_D is the doping density of CdS; A is the device area; $\varepsilon_{r,n}$ and $\varepsilon_{r,p}$ are the relative permittivity of CdS and Sb_2Se_3, respectively; C_0 and C_1 are two quadratic fitting parameters derived from the *C–V* curves and W_d is the depletion width of the device.

The relationship between the depletion width (W_d)and the built-in voltage (V_{bi}) can be estimated by the following equation [10]:

$$W_d = \sqrt{\frac{2\varepsilon_p\varepsilon_n(N_A+N_D)^2}{qN_AN_D(\varepsilon_pN_A+\varepsilon_nN_D)}V_{bi}} \tag{6-4}$$

where q is the elementary charge, ε_p and ε_n are the permittivity, and N_A and N_D are the acceptor density and donor density in Sb_2Se_3 and CdS, respectively.

Supplementary Note7:

Deep-level transient spectroscopy (DLTS) is vital to gain insights into bulk defect properties, including defect concentration, type, and defect energy level of a

photovoltaic device. The corresponding parameters can be derived by the following equation [11]:

$$\ln\left(\tau_e \upsilon_{th,n} N_C\right) = \frac{E_C - E_T}{k_B T} - \ln(X_n \sigma_n) \quad (7\text{-}1)$$

$$\ln\left(\tau_e \upsilon_{th,p} N_V\right) = \frac{E_T - E_V}{k_B T} - \ln(X_p \sigma_p) \quad (7\text{-}2)$$

Where N_C, N_V is conduction band state density and valence band state density, respectively. τ_e is the emission time constant, X_n and X_p are the entropy factor for election and hole, $\upsilon_{th,n}$ and $\upsilon_{th,p}$ is the thermal velocity.

Supplementary Note8:

The transient dynamics were extracted from pseudo-color TAS and fitted by the bi-exponential equation [5]:

$$y = A_1 e^{\left(-\frac{x}{\tau_1}\right)} + A_2 e^{\left(-\frac{x}{\tau_2}\right)} \quad (8\text{-}1)$$

The average lifetime τ_{ave} was estimated from the fitting parameters according to the following equation:

$$\tau_{ave} = \sum A_i \tau_i^2 \Big/ \sum A_i \tau_i \quad (8\text{-}2)$$

Supplementary Figures

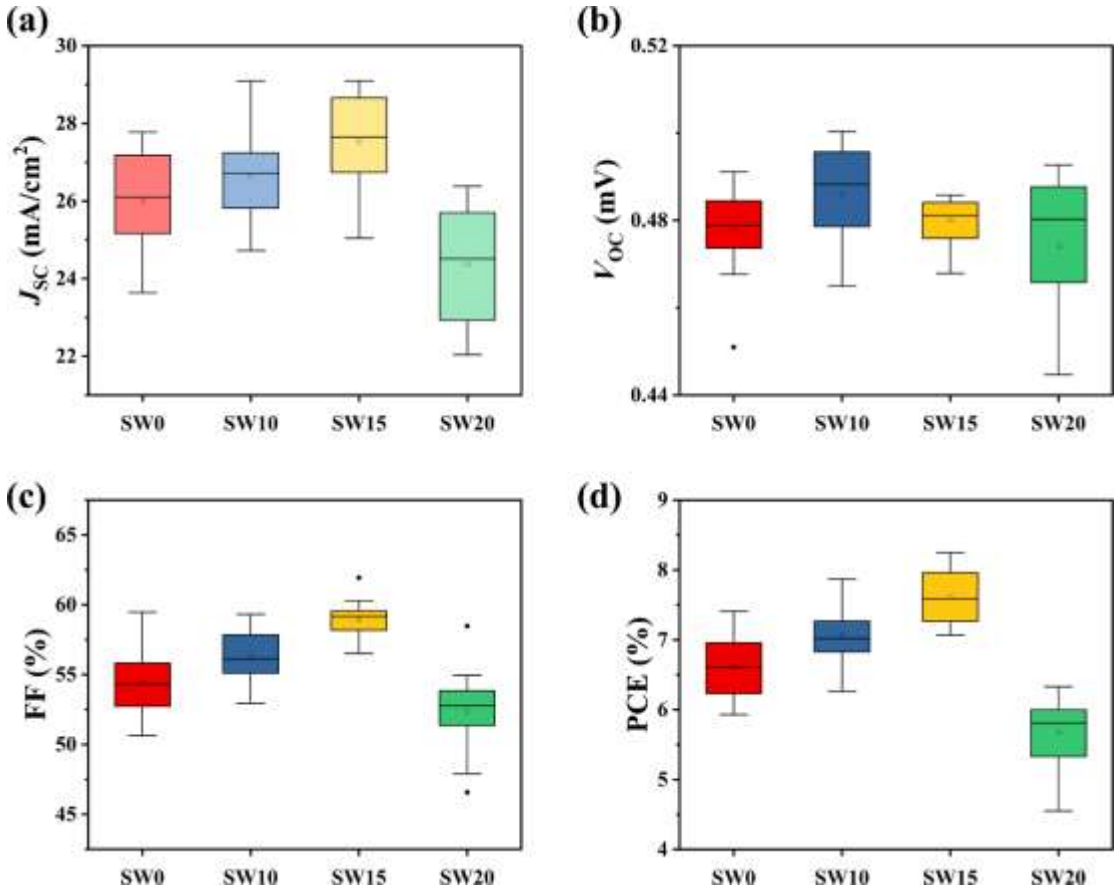

Figure S1 Statistical box diagrams of photovoltaic parameters of the devices with different thicknesses WO_3 layer: (a) J_{SC}, (b) V_{OC}, (c) FF, (d) PCE. Twenty cells were selected for each sample for analysis.

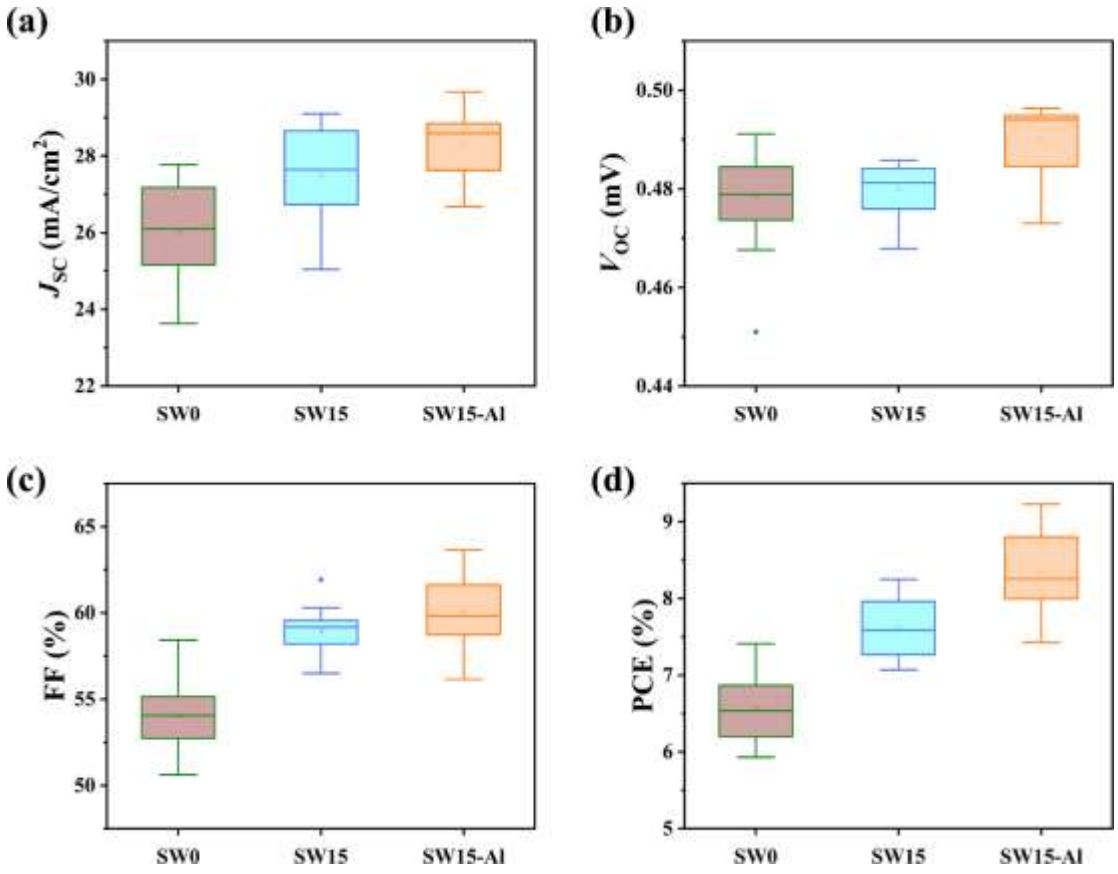

Figure S2 Statistical box diagrams of photovoltaic parameters of three devices: (a) J_{SC}, (b) V_{OC}, (c) FF, (d) PCE. Twenty cells were selected for each sample for analysis.

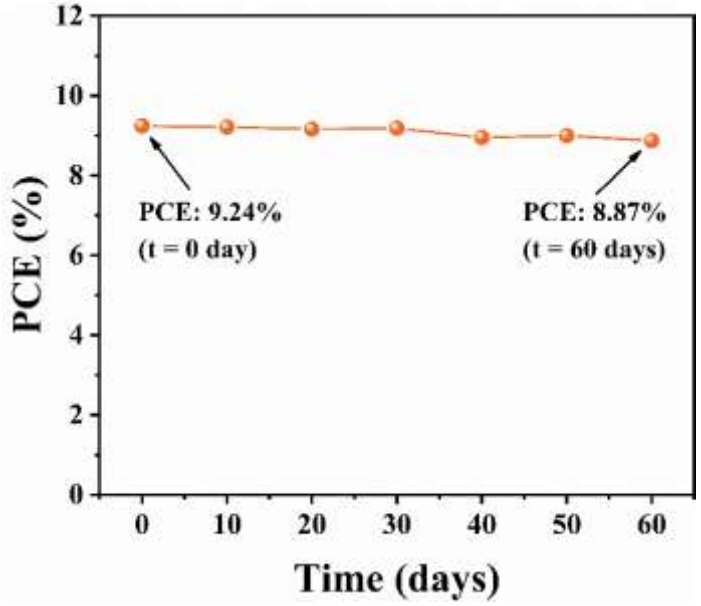

Figure S3 PCE evolution of the champion device after 60 days storage in air ambient without special encapsulation.

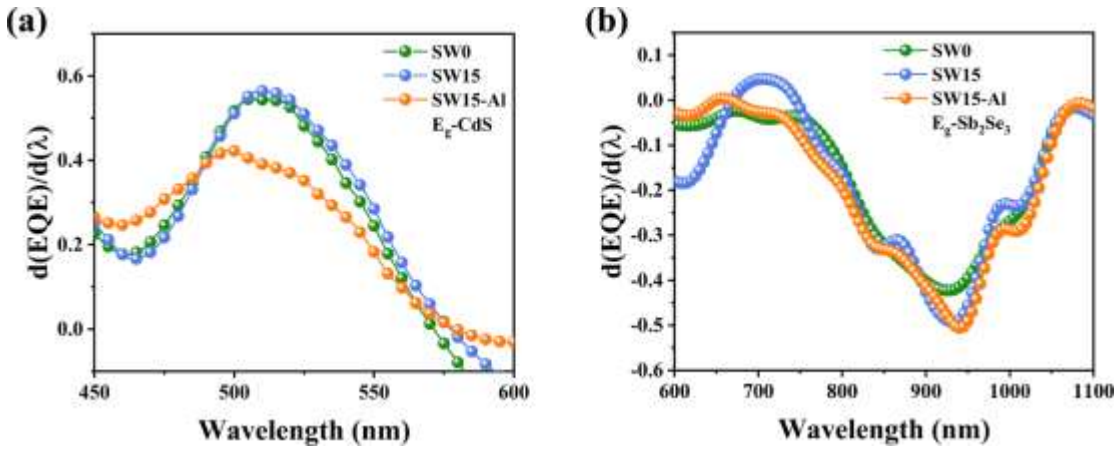

Figure S4 The E_g values of (a) CdS and (b) Sb_2Se_3 obtained from EQE spectra.

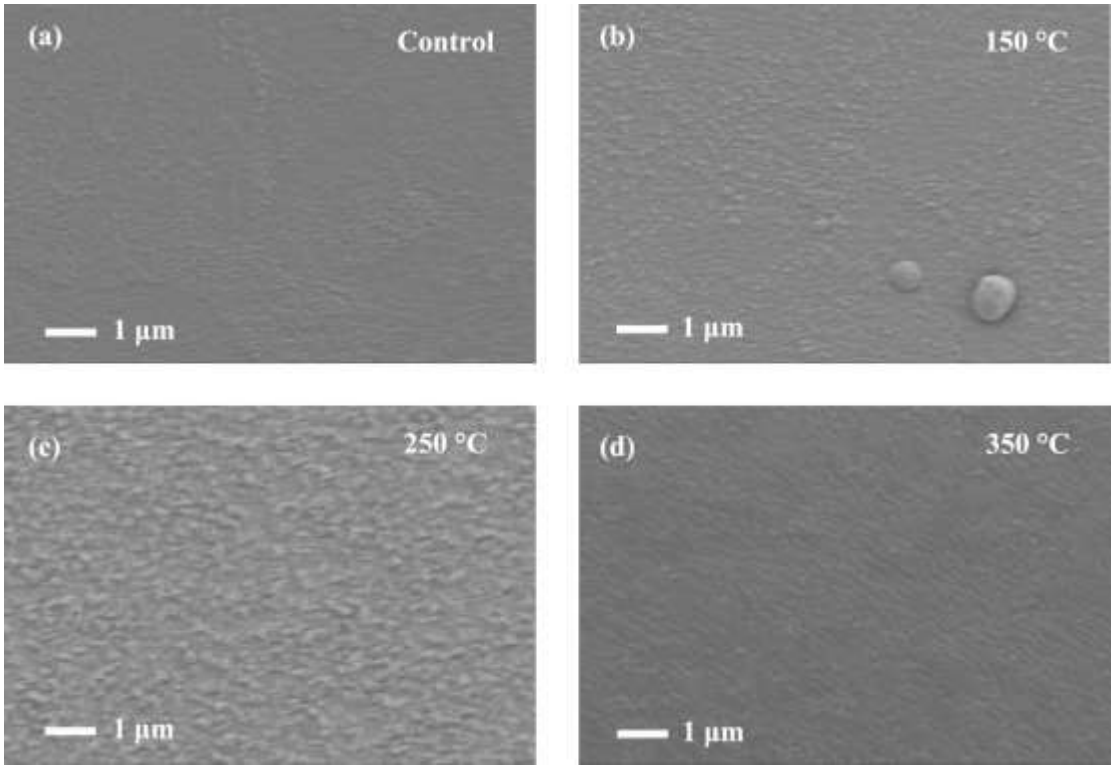

Figure S5 Top-view SEM images of Sb precursor films with different substrate temperatures. (a) At room temperature. (b) At 150 °C. (c) At 250 °C. (d) At 350 °C.

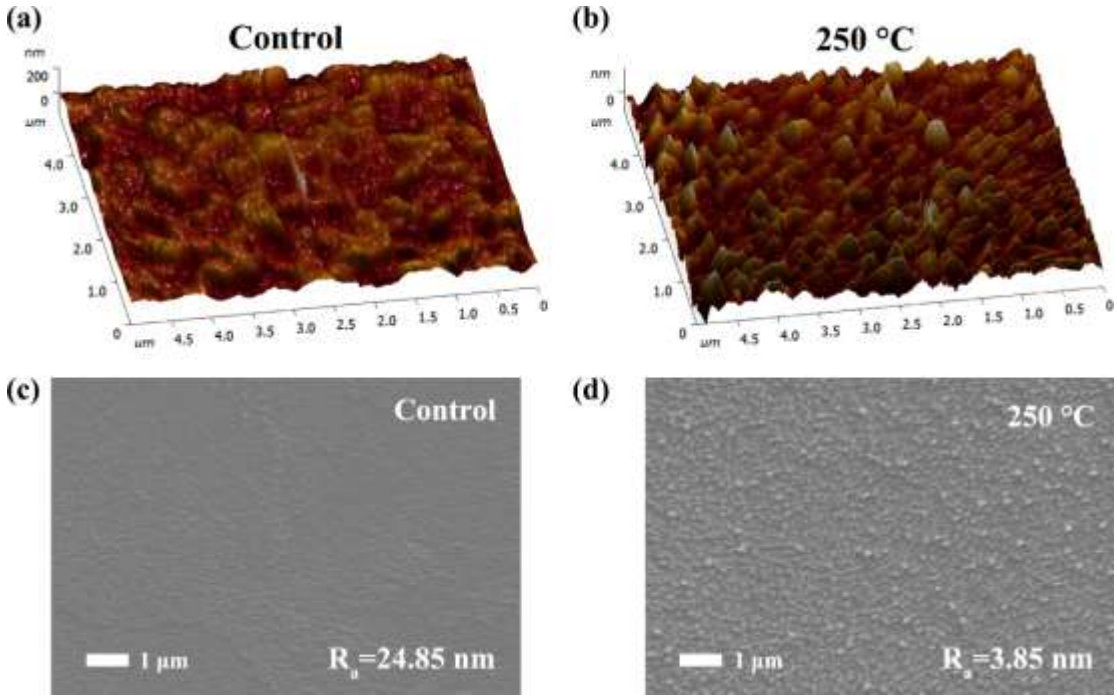

Figure S6 (a) The AFM images of the pristine Sb precursor films. (b) The AFM images of the Sb precursor films with 250 ℃ substrate temperature. (c) The SEM images of the pristine Sb precursor films. (d) The SEM images of the Sb precursor films with 250 ℃ substrate temperature.

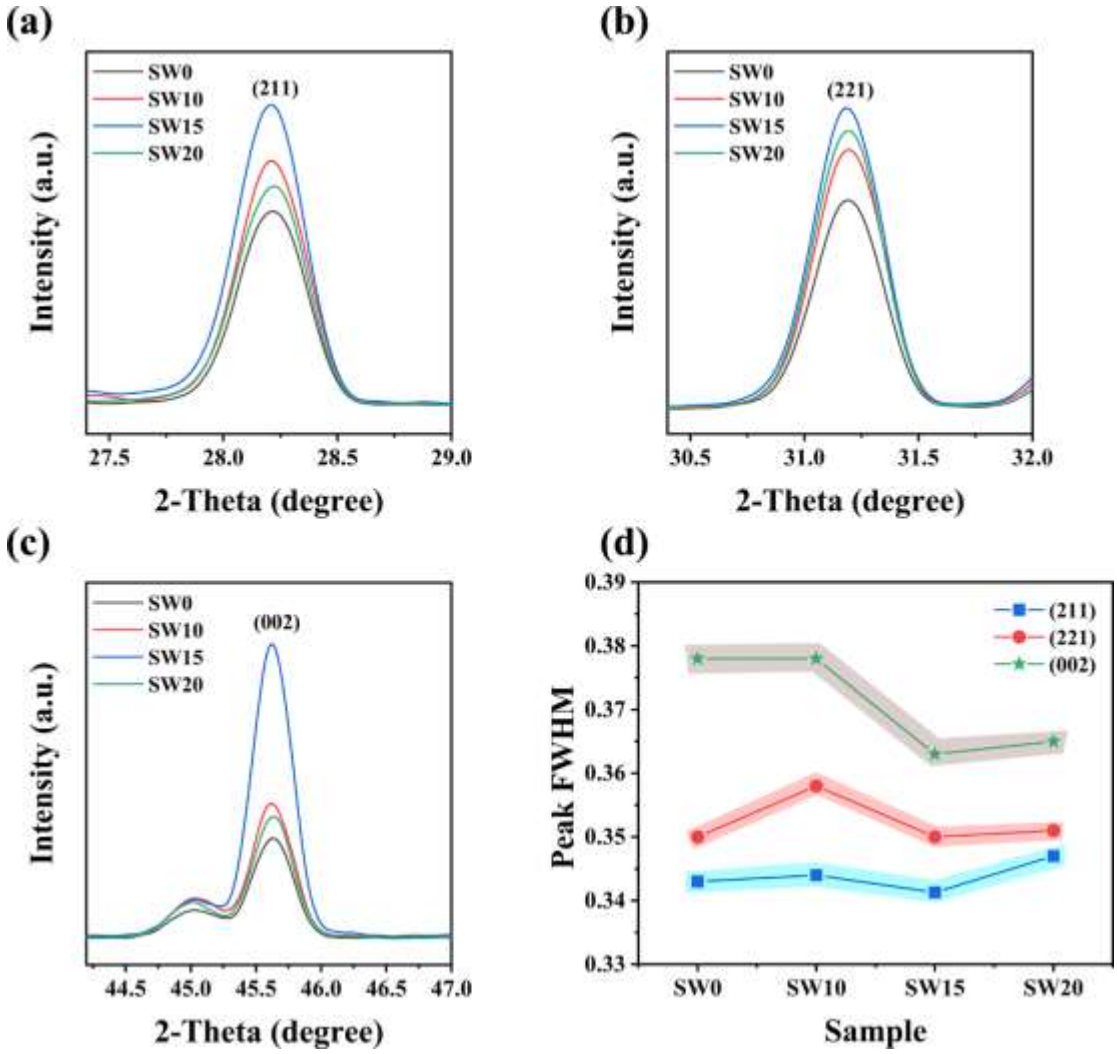

Figure S7 (a) The enlarged XRD patterns of the (211) peak. (b) The enlarged XRD patterns of the (221) peak. (c) The enlarged XRD patterns of the (002) peak. (d) FWHM values of the (211), (221), and (002) peaks by Gaussian fitting for the Sb_2Se_3 absorber layer with different thicknesses of WO_3 layers.

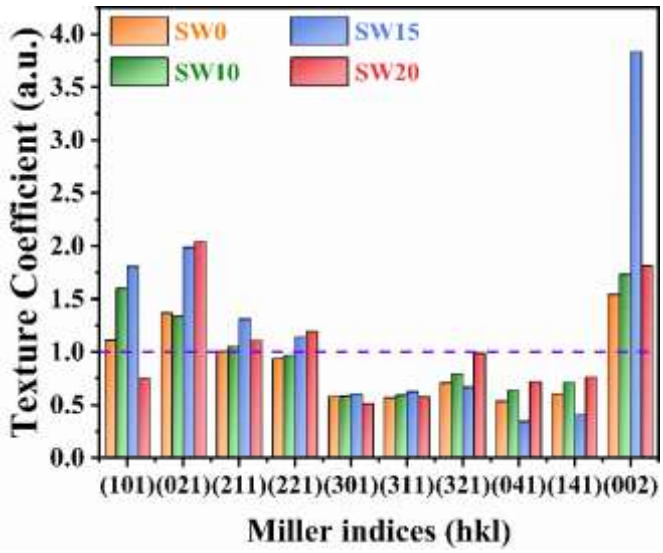

Figure S8 Texture coefficients of the Sb_2Se_3 thin films fabricated with different thicknesses of WO_3 layers.

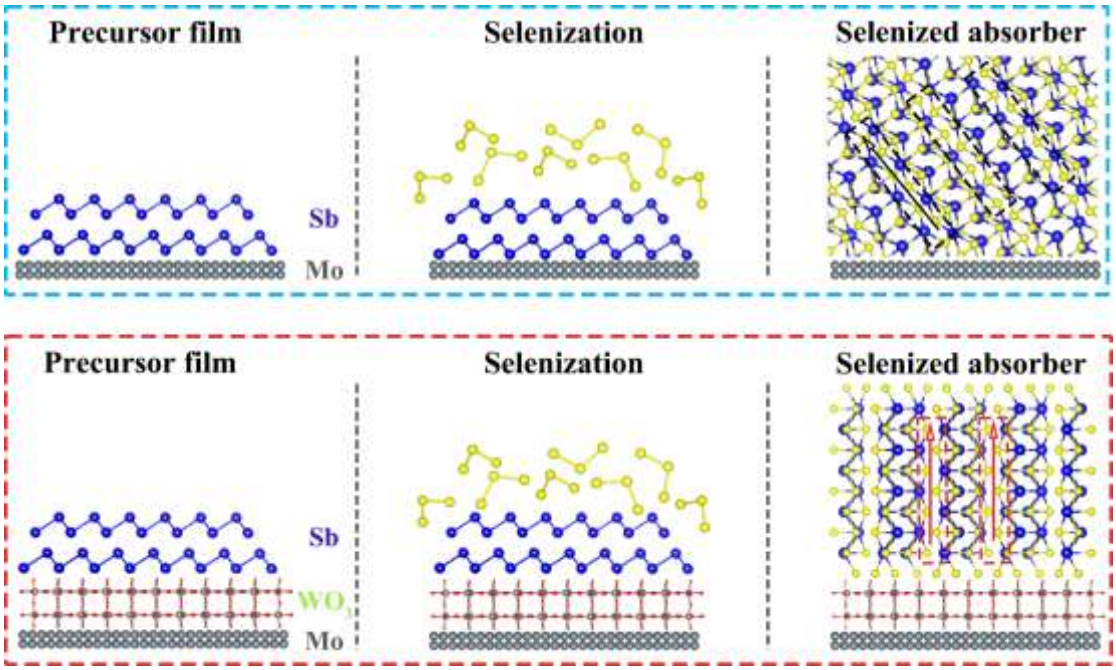

Figure S9 Schematic diagram for the selenization process with or without buried interface modulation.

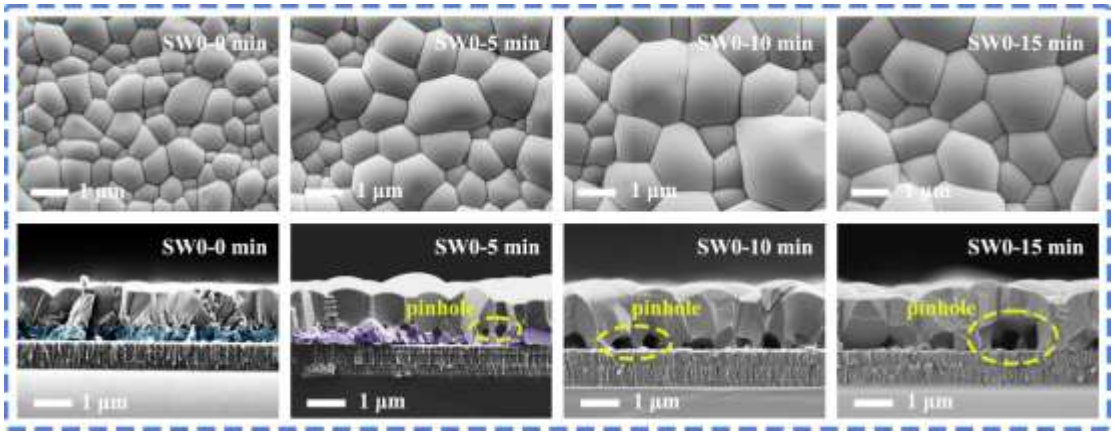

Figure S10 Surface morphology SEM images and cross-sectional SEM images of the Sb_2Se_3 (SW0) films at different selenization times.

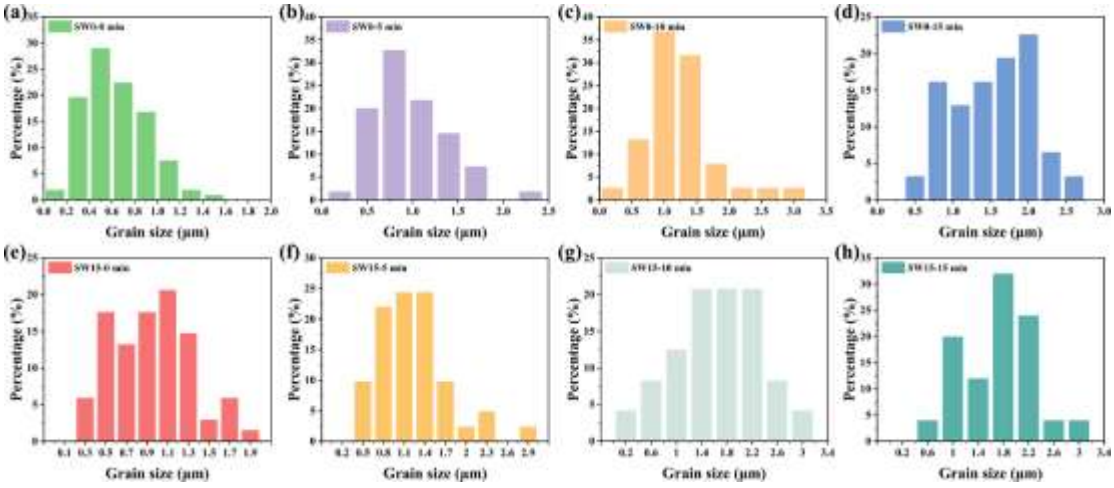

Figure S11 The detailed frequency histograms versus grain size distribution for SW0 films selenized at (a) 0 min, (b) 5 min, (c) 10 min, and (d) 15 min. The detailed frequency histograms versus grain size distribution for SW15 films selenized at (e) 0 min, (f) 5 min, (g) 10 min, and (h) 15 min.

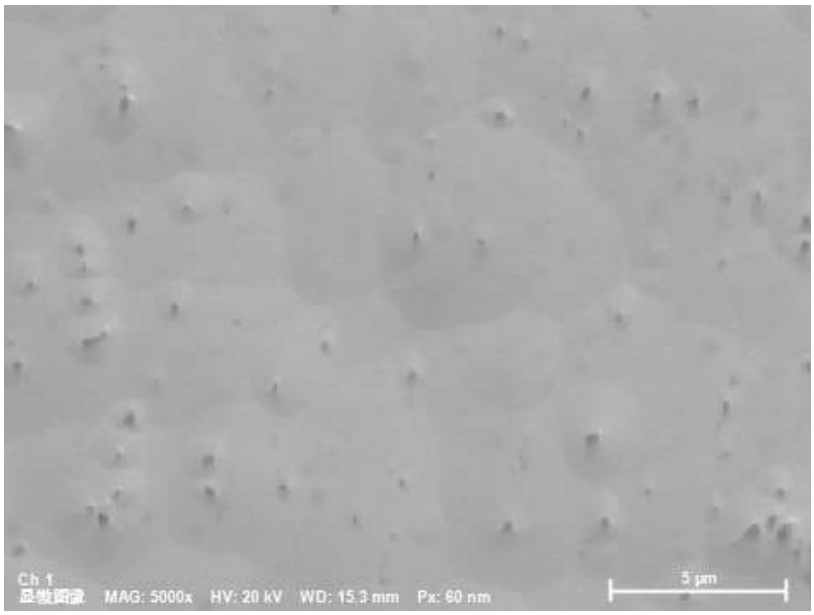

Figure S12 Microtopography image of the SW15 film of the EBSD measurement.

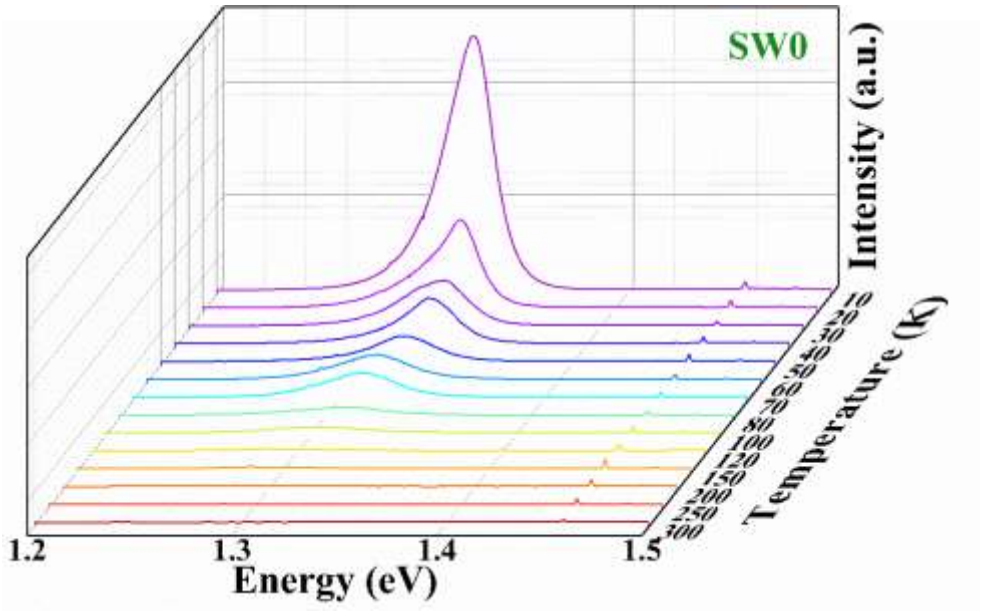

Figure S13 Temperature-dependent PL curves of SW0 film.

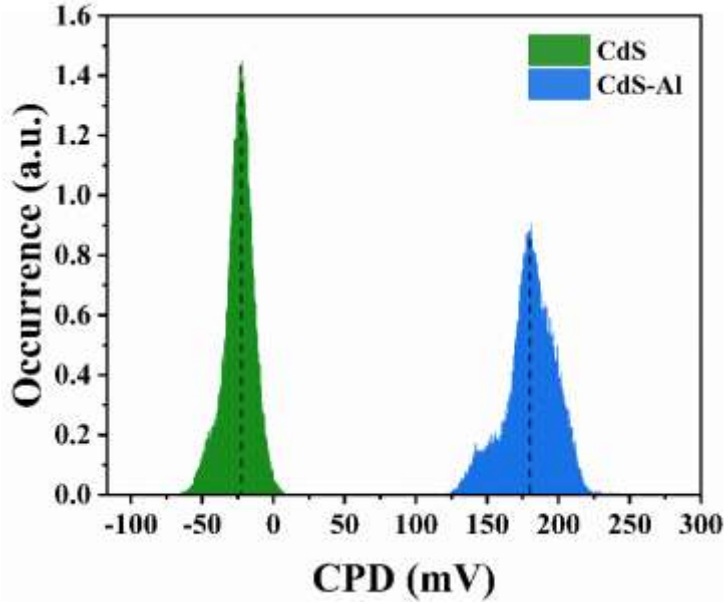

Figure S14 Contact potential difference (CPD) distribution of CdS and CdS-Al films.

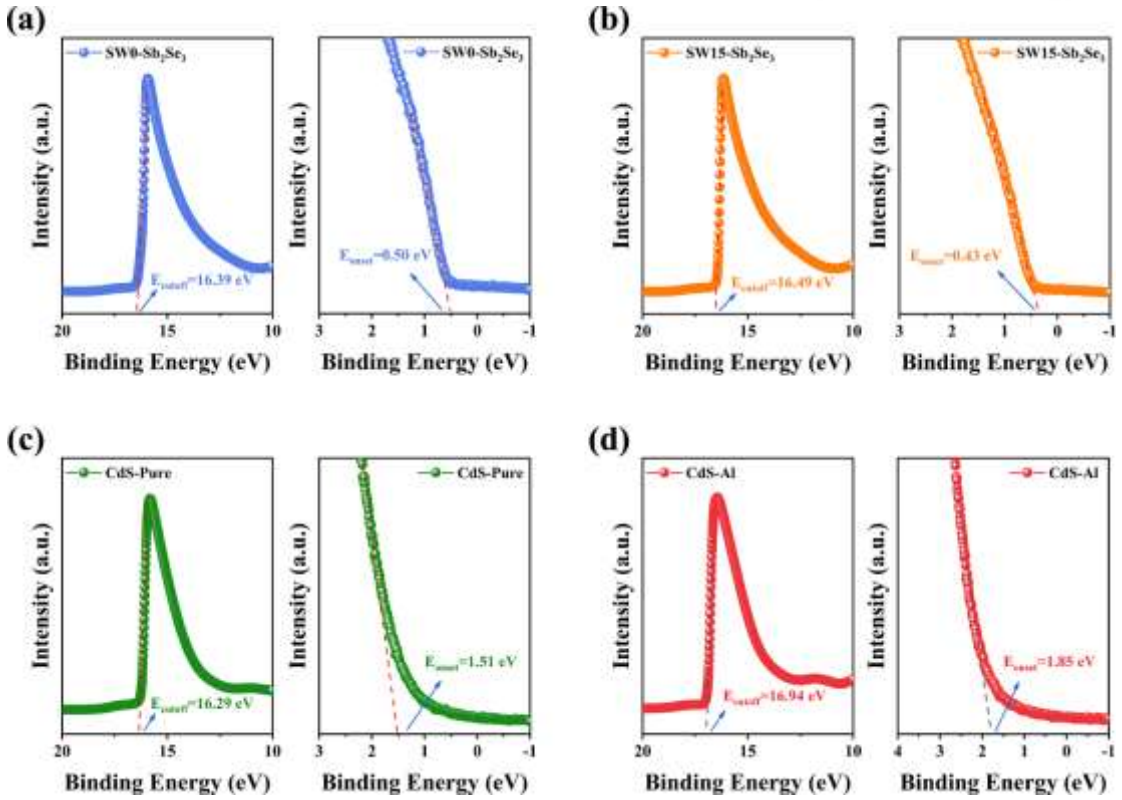

Figure S15 Ultraviolet photoelectron spectroscopy (UPS) results of the (a) SW0 sample, (b) SW15 sample, (c) pristine CdS sample, and (d) CdS-Al sample.

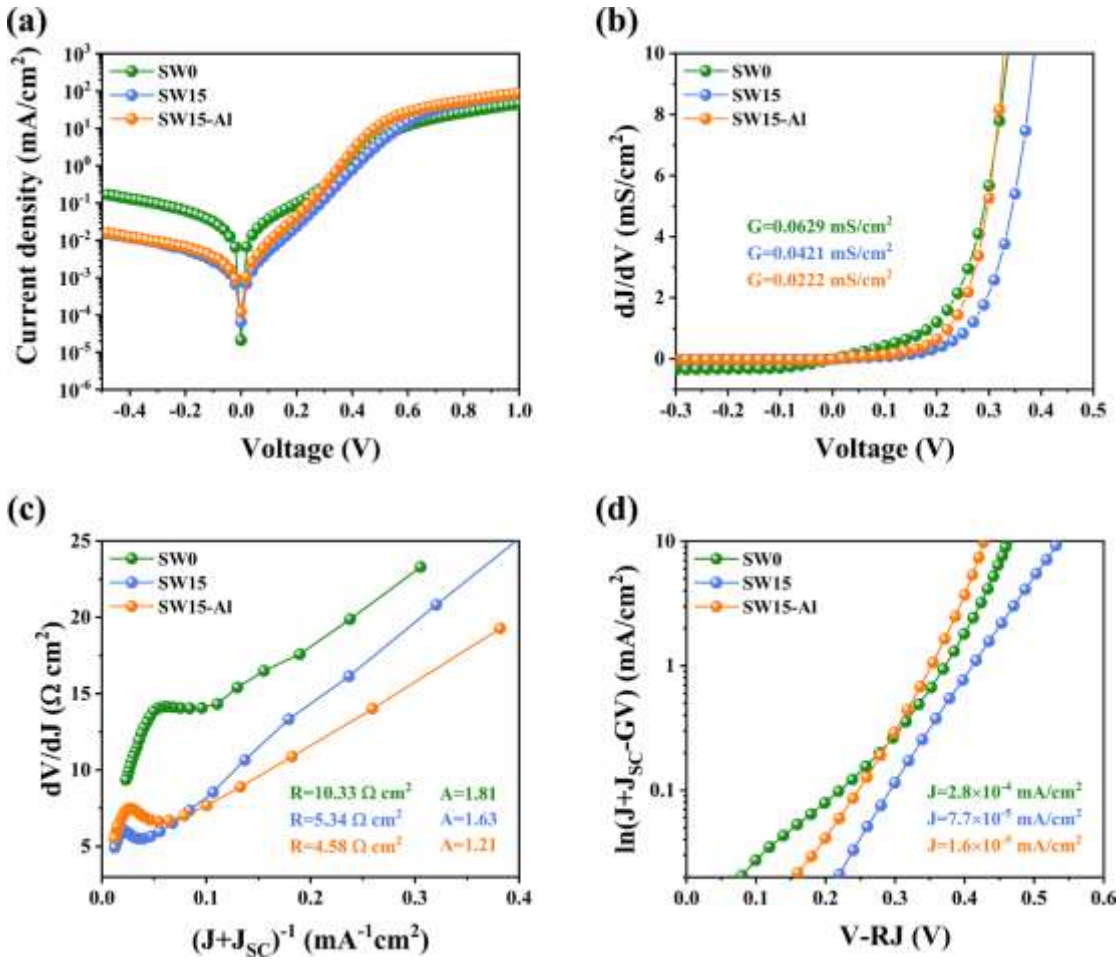

Figure S16 Electrical behaviors of the three devices: (a) dark *J*-*V* curves, (b) shunt conductance *G* characterizations, (c) series resistance *R* and ideality factor *A* characterizations, (d) reverse saturation current density J_0 characterizations.

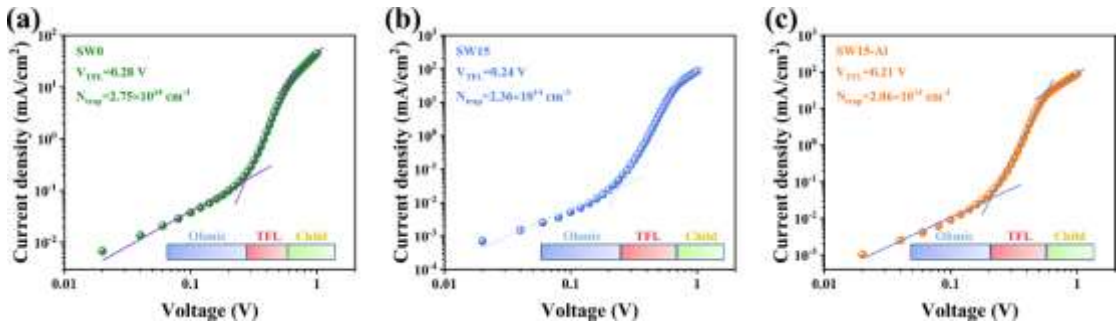

Figure S17 Logarithmic *J-V* curves of the (a) SW0, (b) SW15, and (c) SW15-Al devices.

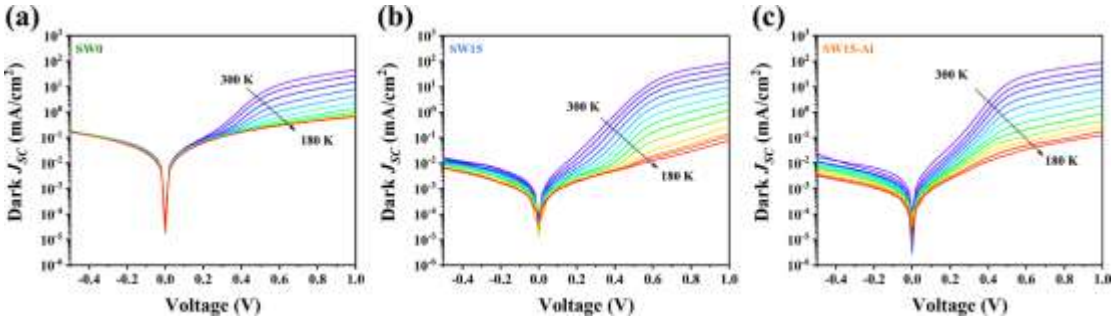

Figure S18 *J-V-T* plots of (a) SW0 device, (b) SW15 device, and (c) SW15-Al device.

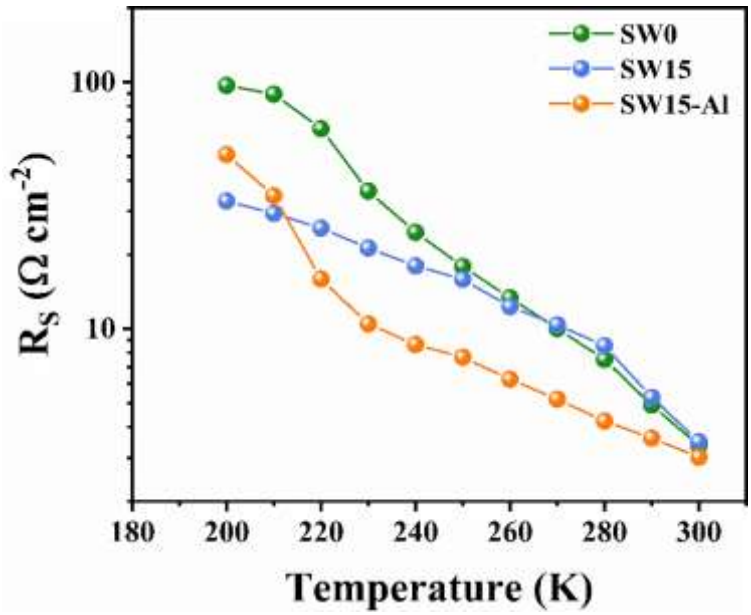

Figure S19 Temperature-dependent R_S of the three devices.

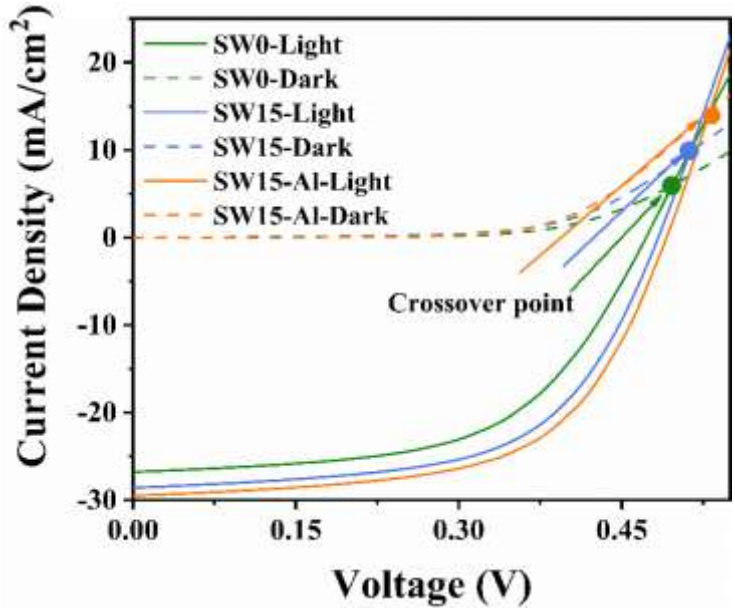

Figure S20 *J-V* curves of the three devices under light and dark states.

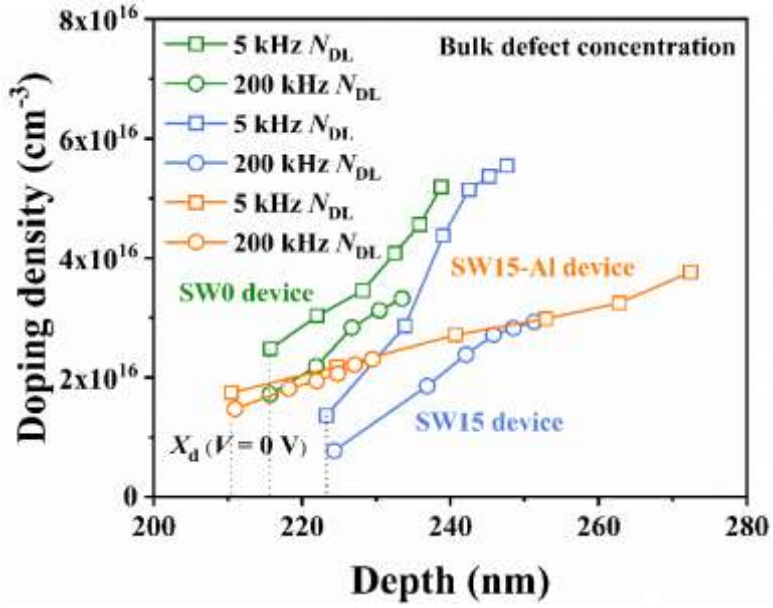

Figure S21 The DLCP profiling of the three devices under high and low frequencies.

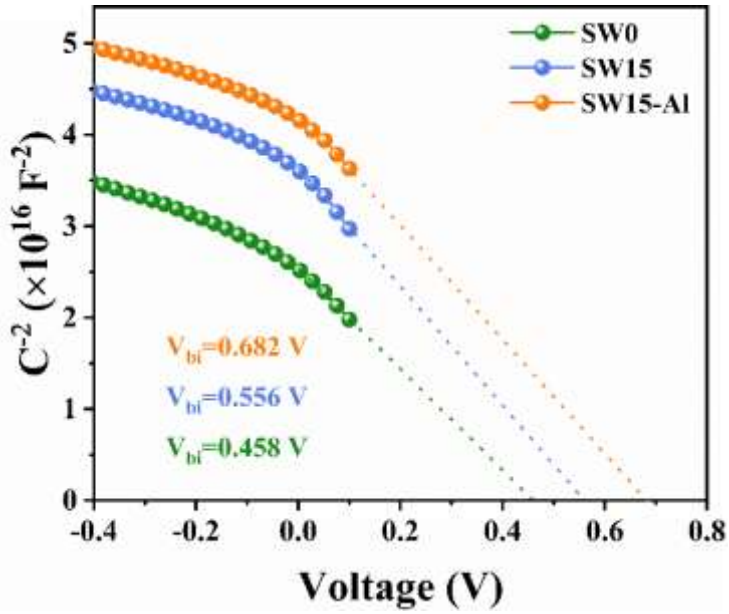

Figure S22 $1/C^2$-V plots of the three devices.

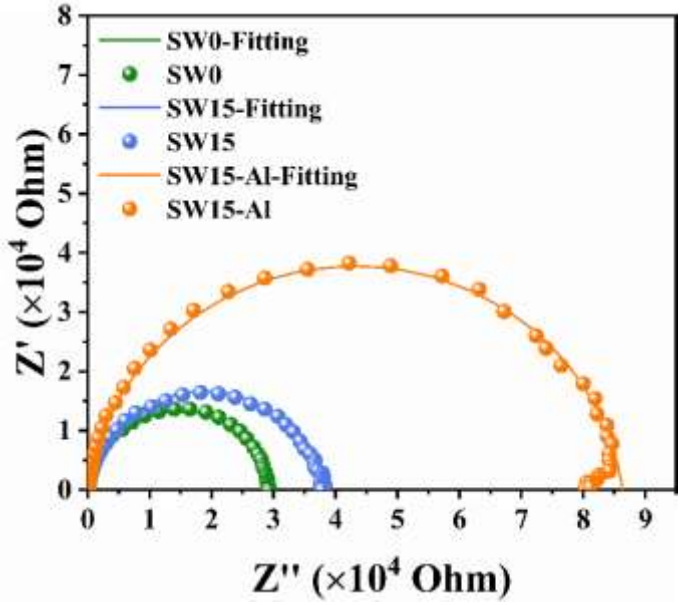

Figure S23 Nyquist plots of the three devices.

Table S1 The band gap of the CdS and Sb_2Se_3 layers derived from the EQE data.

Sample	The band gap of the CdS layer (eV)	The band gap of the Sb_2Se_3 layer (eV)
SW0	2.43	1.35
SW15	2.43	1.32
SW15-Al	2.48	1.32

Table S2 Results of the EIS measurement.

	SW0	SW15	SW15-Al
R_S (Ω)	101.3	10.48	5.644
R_{rec} (Ω)	29574	86308	173450
τ_n (ms)	0.807	2.12	2.87

Reference

[1] P. Fan, G. J. Chen, S. Chen, Z. H. Zheng, M. Azam, N. Ahmad, Z. H. Su, G. X. Liang, X. H. Zhang and Z. G. Chen, *ACS Appl. Mater. Interfaces*, **2021**, 13, 46671-46680.

[2] G. Liang, M. Chen, M. Ishaq, X. Li, R. Tang, Z. Zheng, Z. Su, P. Fan, X. Zhang and S. Chen, *Adv. Sci.*, **2022**, 9, 2105142.

[3] Y. Luo, G. Chen, S. Chen, N. Ahmad, M. Azam, Z. Zheng, Z. Su, M. Cathelinaud, H. Ma, Z. Chen, P. Fan, X. Zhang and G. Liang, *Adv. Funct. Mater.*, **2023**, 33, 2213941.

[4] S. Wang, Y. Zhao, L. Yao, C. Li, J. Gong, G. Chen, J. Li and X. Xiao, *Sci. Bull.*, **2022**, 67,

263-269.

[5] W. Lian, R. Cao, G. Li, H. Cai, Z. Cai, R. Tang, C. Zhu, S. Yang and T. Chen, *Adv. Sci.*, **2022**, 9, 2105268.

[6] Y. Zhao, S. Wang, C. Li, B. Che, X. Chen, H. Chen, R. Tang, X. Wang, G. Chen, T. Wang, J. Gong, T. Chen, X. Xiao and J. Li, *Energy Environ. Sci.*, **2022**, 15, 5118-5128.

[7] G. X. Liang, Y. D. Luo, S. Chen, R. Tang, Z. H. Zheng, X. J. Li, X. S. Liu, Y. K. Liu, Y. F. Li, X. Y. Chen, Z. H. Su, X. H. Zhang, H. L. Ma and P. Fan, *Nano Energy*, **2020**, 73, 104806.

[8] O. Gunawan, T. K. Todorov and D. B. Mitzi, *Appl. Phys. Lett.*, **2010**, 97, 233506.

[9] Y. Zhao, Z. Yu, J. Hu, Z. Zheng, H. Ma, K. Sun, X. Hao, G. Liang, P. Fan, X. Zhang and Z. Su, *J. Energy Chem.*, **2022**, 75, 321-329.

[10] R. Tang, S. Chen, Z. H. Zheng, Z. H. Su, J. T. Luo, P. Fan, X. H. Zhang, J. Tang and G. X. Liang, *Adv. Mater.*, **2022**, 34, 2109078.

[11] R. Tang, X. Wang, W. Lian, J. Huang, Q. Wei, M. Huang, Y. Yin, C. Jiang, S. Yang, G. Xing, S. Chen, C. Zhu, X. Hao, M. A. Green and T. Chen, *Nat. Energy*, **2020**, 5, 587-595.